Association Aéronautique et Astronautique de France

60th 3AF International Conference on Applied Aerodynamics
23 — 25 February 2026, Paris – France

AERO2026-58

Characterization of static and dynamic stall noise of a NACA0012 airfoil using the Lattice Boltzmann Method

Milo Grimberg(1),(2),*, Benjamin Cotté(3), Emmanuel Jondeau(4), Lucien Vienne(4),Vincent Clair(1), Miguel Pestana(2), Jérôme Boudet(1)

(1)Ecole Centrale de Lyon, CNRS, Universite Claude Bernard Lyon 1, INSA Lyon, LMFA, UMR5509, 69130, Ecully, France
(2)Safran Aircraft Engines, Réau, 77550 Moissy-Cramayel, France
(3)Institute of Mechanical Sciences and Industrial Applications (IMSIA), ENSTA, CNRS, EDF, Institut Polytechnique de Paris, France
(4)CNRS, Ecole Centrale de Lyon, INSA Lyon, Universite Claude Bernard Lyon 1, LMFA, UMR5509, 69130, Ecully, France
**Corresponding author: milo.grimberg@ec-lyon.fr*

23 — 25 February 2026

ABSTRACT

The prediction of aerodynamic and aeroacoustic phenomena associated with airfoil stall remains a challenging task due to the strong flow unsteadiness, large-scale separation, and broadband noise generation involved. In this study, the Lattice Boltzmann Method (LBM) is assessed for the simulation of static and dynamic stall noise of a NACA0012 airfoil by direct comparison with experimental data obtained during a dedicated measurement campaign [1].

Numerical simulations are performed at a Reynolds number of $Re_c = 6.25 \times 10^5$ and a Mach number of $Ma = 0.21$ for both fixed and periodically pitching configurations. Static simulations cover angles of attack from $0°$ to $24°$, while the dynamic case consists of a sinusoidal pitching motion at 4 Hz at a mean angles of $15°$ with an amplitude of $\pm 7°$. The numerical results are compared to experimental measurements of pressure coefficient distributions, lift coefficients, wall-pressure spectra, and far-field noise spectra.

For the static configuration, the LBM simulations reproduce the main aerodynamic trends observed experimentally across pre-stall and post-stall regimes. A systematic offset between numerical and experimental results is identified and attributed to a difference between the nominal geometric angle of attack and the effective aerodynamic incidence. Once this offset is taken into account, good agreement is obtained in terms of pressure distributions, lift polar evolution, and far-field noise levels. In the dynamic configuration, the LBM captures the characteristic lift hysteresis associated with dynamic stall, as well as the temporal modulation of aerodynamic and acoustic quantities throughout the pitching cycle.

In addition to integral metrics, the analysis of instantaneous fields provides qualitative insight into the spatial localization of dominant acoustic source regions, highlighting the role of the boundary layer and the trailing edge in noise radiation. Overall, the results demonstrate that the Lattice Boltzmann Method constitutes a reliable approach for predicting the aerodynamic and aeroacoustic response of airfoils under static and dynamic stall conditions at moderate Mach numbers.

Keywords: Airfoil noise, Pitching airfoil, LBM, Stall noise, Static stall, Dynamic stall

1. INTRODUCTION

Airfoil stall remains a major challenge in aerodynamics and aeroacoustics due to its strong impact on aerodynamic performance, unsteady loading, and noise generation. As the angle of attack increases, boundary-layer separation develops on the airfoil, leading to a loss of lift and to the emergence of large-scale unsteady flow structures. These flow features are responsible for significant pressure fluctuations and enhanced broadband noise emission, while dynamic stall conditions are known to generate strongly modulated acoustic signatures [2, 3, 4].

Recent experimental work, such as the database published by Raus et al. [5, 6], has provided detailed measurements of airfoil stall noise in controlled conditions. The experimental database was obtained in the framework of the PIBE project [1]. Such datasets constitute valuable references for the validation of numerical methods, especially in flow regimes where separation and unsteadiness play a dominant role.

The present work relies on measurements obtained during the same experimental campaign, at a specific operating point that has not been previously published: a Reynolds number of $Re_c = 6.25 \times 10^5$ and a Mach number of $Ma = 0.21$. This operating point is more representative of realistic flow conditions in wind energy application or low speed turbomachinery. It differs from the low-Mach-number configurations commonly reported in the literature, thereby offering an opportunity to further assess the robustness of numerical approaches.

In this context, the Lattice Boltzmann Method (LBM) has emerged as a promising alternative to conventional Navier–Stokes solvers for aeroacoustic applications by resolving large eddy scales. Thanks to its kinetic formulation and low numerical dissipation, LBM is well suited for the simulation of unsteady flows involving separation, vortex dynamics, and acoustic wave propagation [7, 8, 9]. However, the validation of LBM in high-Reynolds-number stall conditions remains limited.

The objective of the present study is to evaluate the ability of an LBM-based solver to reproduce the aerodynamic and acoustic trends observed experimentally. Two complementary conditions are considered. First, static simulations are performed for angles of attack ranging from 0° to 24° in order to assess the consistency of the predicted pressure distributions, integrated lift coefficients, and far-field noise levels. Second, a dynamic case is investigated in which the airfoil undergoes a sinusoidal pitching motion at 4 Hz about a mean angle of 15° with an amplitude of ±7°, leading to the development of dynamic stall. Dynamic stall is a key unsteady aerodynamic phenomenon encountered in many engineering applications, such as in turbomachinery, wind turbines, and more generally rotors, where blades operate under periodically varying incidence. It is characterized by delayed flow separation, the formation of large-scale vortical structures, and strong unsteady loading, which in turn generate pronounced aeroacoustic emissions. Studying dynamic stall is therefore essential to assess the capability of numerical methods to capture realistic unsteady flow physics and their acoustic signatures under representative operating conditions.

Rather than providing an exhaustive physical analysis of stall mechanisms, the focus of this work is placed on the comparison between numerical predictions and experimental observations. The results aim to establish if the LBM approach is capable of reproducing the key aerodynamic and acoustic features associated with static and dynamic stall, thereby providing a solid basis for its application to more complex unsteady aeroacoustic problems.

2. NUMERICAL METHOD: LATTICE BOLTZMANN METHOD AND HRR COLLISION MODEL

The flow simulations are performed using the Lattice Boltzmann solver ProLB (v3.4) [10], based on a weakly compressible formulation of the Lattice Boltzmann Method (LBM) and using the Hybrid Recursive Regularization (HRR) collision operator [11, 12].

The LBM solves for a set of discrete particle distribution functions $f_i(\mathbf{x},t)$ associated with a finite set of discrete velocities $\mathbf{c}_i$. The evolution equation reads:

$$f_i(\mathbf{x}+\mathbf{c}_i\Delta t,\, t+\Delta t) = f_i(\mathbf{x},t) + \Omega_i(\mathbf{x},t) \tag{1}$$

where $\mathbf{c}_i$ the sound speed vector, $\mathbf{x}$ the coordinate vector, Δ_t the time step and Ω_i the collision operator.

The macroscopic fields are recovered from the zeroth and first order moments:

$$\rho = \sum_i f_i, \qquad \rho\mathbf{u} = \sum_i f_i\mathbf{c}_i \tag{2}$$

and the pressure follows the isothermal relation

$$p = c_s^2\rho \tag{3}$$

where ρ denotes the density, $\mathbf{u}$ the velocity vector, c_s is the lattice sound speed.

The classical single-relaxation-time (BGK) operator,

$$\Omega_i^{BGK} = -\frac{1}{\tau}\left(f_i - f_i^{\mathrm{eq}}\right) \tag{4}$$

suffers from stability issues at high Reynolds numbers and in strongly unsteady or separated flows. To improve robustness and accuracy, ProLB employs a regularized multi-moment formulation based on Hermite polynomial reconstruction. [11]

In the HRR model, the distribution function is decomposed into equilibrium and non-equilibrium parts:

$$f_i = f_i^{\mathrm{eq}} + f_i^{\mathrm{neq}} \tag{5}$$

The non-equilibrium component is replaced by a regularized expression $f_i^{\mathrm{neq,reg}}$ built from a recursive reconstruction of Hermite moments, leading to the HRR collision operator [12]:

$$\Omega_i^{HRR} = -\frac{1}{\tau}\left(f_i - f_i^{\text{eq}} - f_i^{\text{neq,reg}}\right) \tag{6}$$

Time integration is obtained via the standard stream–collide procedure with exact streaming. Because compressibility is intrinsically modeled by the discrete kinetic equation, no additional acoustic modeling or hybrid coupling is required.

3. METHODOLOGY FOR EXPERIMENT–SIMULATION COMPARISON

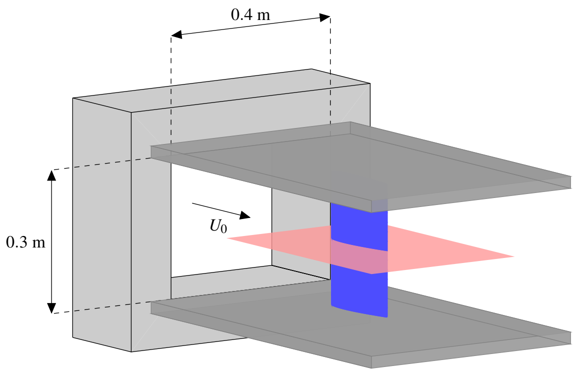

Figure 1. Schematic of the experimental setup.

The present section describes the methodology adopted to ensure a consistent comparison between the unpublished experimental reference issued from the campaign of Raus et al. [5, 6] and the numerical results obtained using the Lattice Boltzmann solver ProLB [10]. Although the full experimental setup involves a three-dimensional airfoil mounted in an open-jet wind tunnel with acoustic instrumentation, the numerical simulation reproduces a short-span slice of the configuration extracted at the mid-span. The following subsections describe the processing of the experimental data, the numerical domain that faithfully reproduces the experimental setup, and the parameters used for aerodynamic and acoustic comparisons.

The experimental configuration corresponds to the wind-tunnel setup described by Raus et al. [5, 6]. A NACA0012 airfoil with a span of 300 mm and a chord of $c = 0.12$ m is mounted between side plates in an open-jet inside an anechoic chamber. Aerodynamic forces are obtained from the integrated pressure distribution, while acoustic measurements rely on far-field microphones, with a reference microphone at $\theta = 90^\circ$ and $r = 2$ m. Fig. 1 shows the experimental configuration. A boundary-layer trip consisting of a 25 mm wide tape is applied on both sides of the airfoil between $x/c = 0.16$ and $x/c = 0.36$ in order to enforce laminar-turbulent transition turbulent boundary layers and prevent laminar tonal noise at low incidence [4].

The numerical simulation represents a "2.5-dimensional" slice extracted at the mid-span location of the experimental airfoil represented by the red plane in Fig. 1. The computational domain extends 2.42 chords upstream, 10 chords downstream, and 10 chords laterally, ensuring negligible interference of outgoing acoustic waves with the boundaries. Fig. 2 illustrates the "2.5-dimensional" computational domain and boundary conditions. The spanwise length is chosen as the maximal vortical structure: $c\sin(\alpha_{\text{max}}) = 0.41 \times c$. Sponge layers are implemented at the inlet and outlet boundaries to damp outgoing hydrodynamic and acoustic fluctuations and minimize wave reflections.

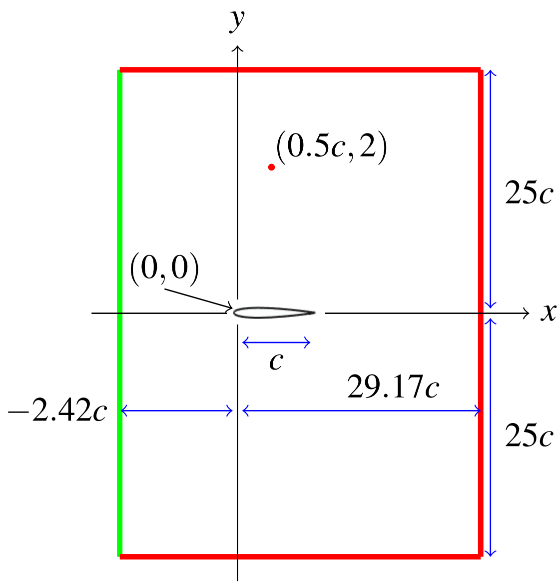

Figure 2. Schematic of the numerical setup. Green line: inlet boundary condition. Red line: outlet boundary condition. z-axis extend to $0.41c$, with frictionless boundary conditions. Red dot: Microphone. *The diagram is not drawn to scale.*

In the dynamic configuration, the pitching motion of the airfoil is imposed numerically through an oscillating inflow jet, designed to reproduce the time-dependent variation of the effective angle of attack. The jet is modeled using a smooth hyperbolic tangent velocity profile in the vertical direction, whose orientation oscillates sinusoidally in time. This formulation ensures a continuous velocity field with controlled shear-layer thickness while avoiding numerical discontinuities at the jet boundaries.

3.1 Mesh convergence on aerodynamics

Te ensure a mesh independent results, a mesh convergence is required. The mesh convergence study is conducted for static cases because the numerical setup is the same between static and dynamic cases. The lift coefficient sensitivity is shown in Fig. 3.

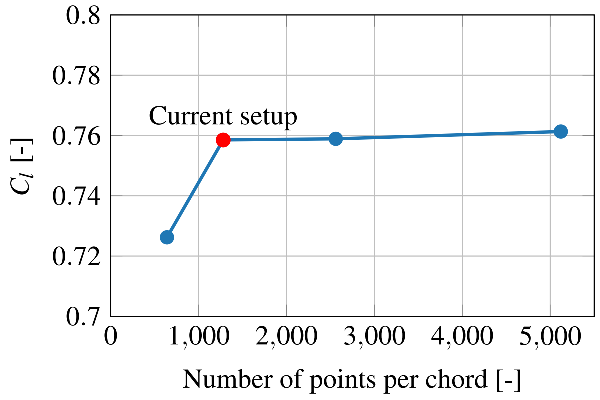

Figure 3. Mesh convergence on lift coefficient at $\alpha = 10°$.

The mesh convergence study shows a minimum mesh size at $d_x = 9.375 \times 10^{-5}$ m yields a converged lift coefficient value. Main characteristics of the reference numerical setup are detailed in Tab. 1 and visualizations of the Cartesian LBM grid are shown in Fig. 4a and Fig. 4b.

Number of nodes	36 000 000
Number of fine equivalent nodes	18 000 000
y^+ at the airfoil wall	< 30
Number of refinement levels	8
d_x at the airfoil wall	9.53×10^{-5} m
d_t at the airfoil wall	1.58×10^{-7} s
Number of convective time	500

Table 1. Characteristics of the LBM grid.

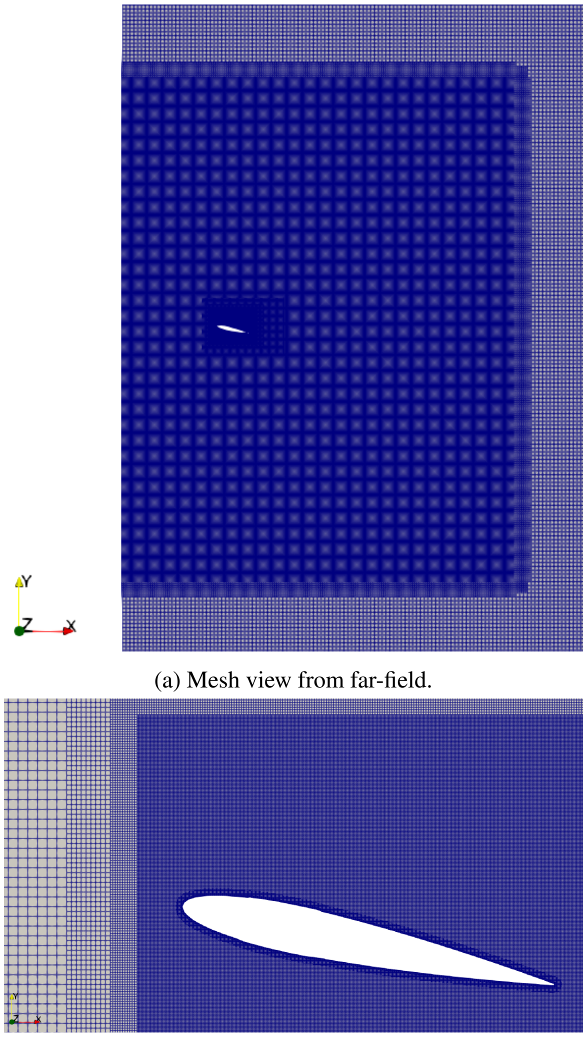

(a) Mesh view from far-field.

(b) Mesh view close to the airfoil.

Figure 4. Illustration of the LBM mesh.

3.2 Angle of attack calibration

Before comparing in details the LBM simulations and the experimental database, it is necessary to assess the consistency of the operating point. During the preliminary analysis of the experimental pressure coefficient distributions, a systematic shift was observed between the expected aerodynamic behavior of the NACA0012 airfoil and the experimental curves for a given geometric angle of attack α_{geo}. Rather than indicating an inconsistency in the data, this observation suggests that the effective aerodynamic angle of attack may differ slightly from the geometric reference.

To investigate this point, the experimental pressure coefficient distribution

$$C_p(x) = \frac{p(x) - p_\infty}{\frac{1}{2}\rho_\infty U_\infty^2}, \quad (7)$$

has been compared with several reference datasets, including: (i) xFoil computations performed at identical Mach and Reynolds numbers, and (ii) the present LBM simulations.

For angles of attack ranging from 0° to 6°, the evolution of the pressure distributions was examined. As recalled in Raus et al. [5, 6], the experimental determination of the pressure distribution at a given geometric angle of attack requires two separate acquisitions, one at a positive α_{geo} and one at a negative α_{geo}, since the airfoil is instrumented on only one side. As a consequence, the suction and pressure sides are not measured simultaneously under identical flow conditions.

The comparison with the numerical references suggests that the experimental pressure distributions correspond to an effective angle of attack shifted with respect to the nominal geometric value. More specifically, for a given reference angle α_{geo}, the suction-side pressure distribution appears consistent with numerical results obtained at approximately $\alpha_{\text{geo}} - 1.2°$, while the pressure-side distribution is closer to results at $\alpha_{\text{geo}} + 1.2°$.

This interpretation is illustrated in Fig. 5, where the experimental pressure distribution reported at $\alpha_{\text{geo}} = 0°$ closely matches the LBM and xFoil results obtained at $\alpha = 1.2°$. A similar trend is observed in Fig. 6 for a nominal angle of attack of 6°.

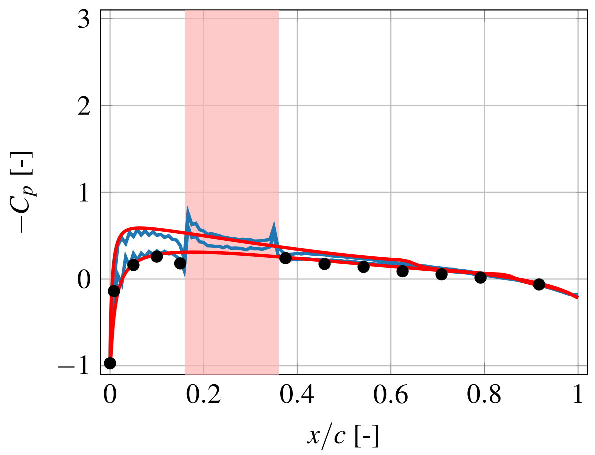

Figure 5. Wall-pressure distribution on the airfoil for: LBM at 1.2° (blue line), XFoil at 1.2° (red line) and experimental data at 0° (●). Trip (pink band).

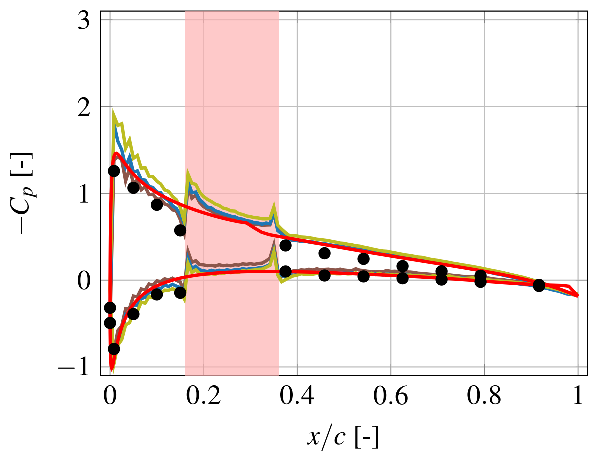

Figure 6. Wall-pressure distribution on the airfoil for: LBM at 5° (brown line), LBM at 6° (blue line), LBM at 7° (yellow line), XFoil at 6° (red line) and experimental data at 6° (●). Trip (pink band).

This systematic offset is interpreted as a geometric offset inherent to the experimental setup, leading to a discrepancy between the nominal geometric angle of attack and the effective flow incidence. Consequently, throughout the remainder of this paper, angles of attack are expressed using the LBM reference angle, which is taken as the effective aerodynamic angle for all subsequent comparisons.

Quantifying this offset is essential for a meaningful comparison between the experimental database of Raus et al. [5, 6] and the present LBM simulations, since both aerodynamic and acoustic quantities are highly sensitive to the effective angle of attack. In particular, the non-simultaneous acquisition of the pressure and suction sides may lead to slight discrepancies in the reconstructed pressure distributions and, consequently, in the derived lift coefficient.

4. AERODYNAMICS AND ACOUSTICS OF A FIXED AIRFOIL

This section presents a comparison between the experimental database and the LBM predictions for a fixed NACA0012 airfoil. The analysis focuses on a limited number of representative angles of attack, selected to illustrate the main aerodynamic regimes, from attached flow to fully separated conditions, as well as their associated acoustic signatures.

4.1 Aerodynamics

4.1.1 Wall-pressure distributions

The aerodynamic validation is first conducted by comparing the pressure coefficient distributions obtained experimentally and numerically at different angles of attack. Wall-pressure distributions constitute a robust metric for assessing airfoil aerodynamic behavior across different flow regimes, from attached flow to stall [13, 14]. The angles are chosen to represent an attached flow regime, the onset of separation and the post-stall conditions.

Fig. 7, Fig. 8 and Fig. 9 shows the C_p distributions for both datasets. The comparison highlights that the LBM simulations reproduce the overall shape of the experimental pressure distributions, including the suction peak, pressure recovery, and the separation-induced plateau. Such features are commonly used to identify separation onset and stall development in both experimental and numerical studies [13, 15]. However, the level of the plateau in Fig. 9 is estimated higher in LBM compared to the experiment. This shift will be investigated in future simulations.

A systematic difference in levels is nevertheless observed, which is consistent with the effective angle-of-attack offset identified in Sec. 3.2. This offset leads to slightly stronger suction levels in the numerical results when compared to the experimental distributions.

Despite this moderate shift, the evolution of the pressure distributions with increasing angle of attack is consistent between the two datasets. This indicates that the main aerodynamic mechanisms governing flow attachment, separation onset, and post-stall behavior are well

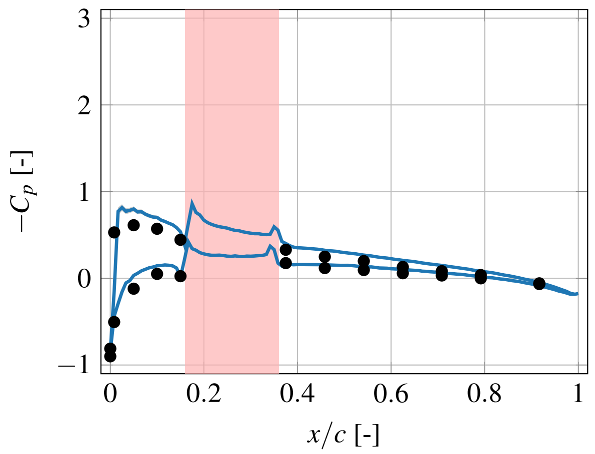

Figure 7. Wall-pressure distribution: comparison between LBM predictions at $\alpha = 3°$ (—) and experimental data at $\alpha = 3°$ (●). Trip ( ) and LBM $C_{p,\mathrm{RMS}}$ envelope ( )

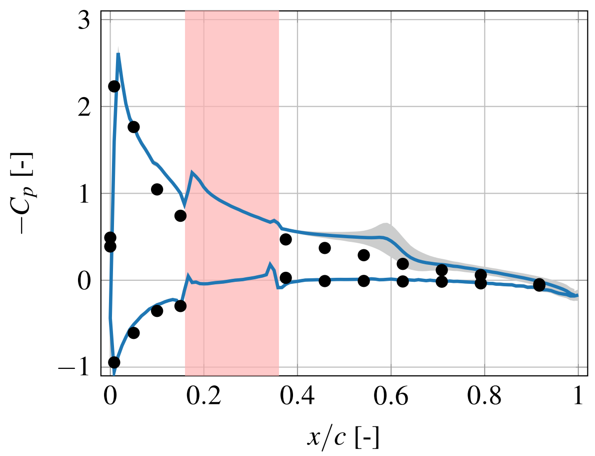

Figure 8. Wall-pressure distribution: comparison between LBM predictions at $\alpha = 9°$ (—) and experimental data at $\alpha = 9°$ (●). Trip ( ) and LBM $C_{p,\mathrm{RMS}}$ envelope ( )

captured by the LBM solver, in agreement with previous LBM-based airfoil studies [16, 17].

4.1.2 Lift evolution

To provide a global aerodynamic assessment, the lift coefficient obtained from the integration of the pressure distributions is compared to the experimental evolution. The lift coefficient is computed as:

$$C_l = -\int_0^1 \left(C_{p,u} - C_{p,l}\right) \mathrm{d}(x/c), \qquad (8)$$

which represents a standard approach for experimental and numerical airfoil characterization [13]. Fig. 10

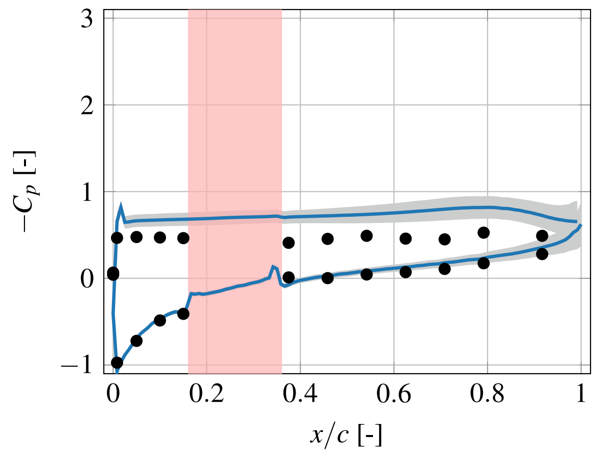

Figure 9. Wall-pressure distribution: comparison between LBM predictions at $\alpha = 18°$ (—) and experimental data at $\alpha = 18°$ (●). Trip ( ) and LBM $C_{p,\mathrm{RMS}}$ envelope ( )

presents the evolution of C_l as a function of the angle of attack for both datasets. The numerical lift curve exhibits a similar slope and stall angle to the experimental ones. The agreement confirms that the LBM solver correctly reproduces the aerodynamic evolution in the attached regime. However, the C_l is slightly overestimated during the separation onset, and more significantly after stall.

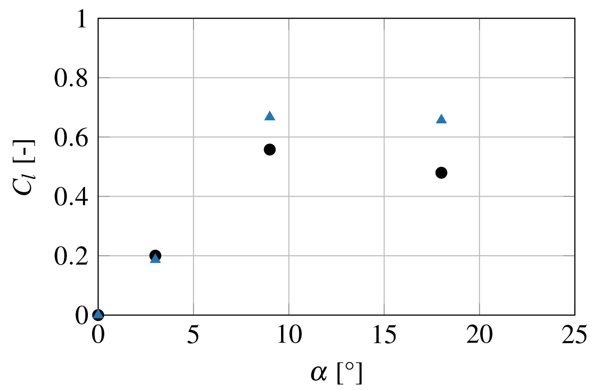

Figure 10. Fixed airfoil lift coefficient as a function of angle of attack: comparison between LBM predictions (▲) and experimental data (●).

4.2 Acoustics

4.2.1 Wall-pressure spectra

The acoustic validation first considers the pressure fluctuations measured on the airfoil wall. In this paper the wall-pressure spectra is shown as the parameter: ϕ_{pp}.

Fig 11 shows a comparison of wall-pressure power spectral densities obtained experimentally and numerically at selected angles of attack.

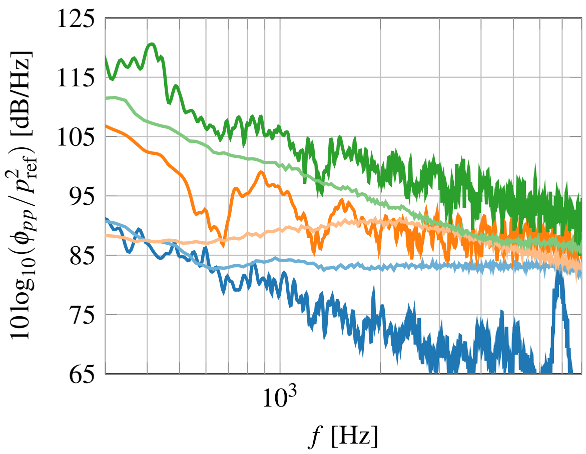

Figure 11. Comparison of wall-pressure spectra on suction side at $x/c = 0.92$, between LBM and experiment at selected static angles of attack. (—) $\alpha = 3°$ LBM, (—) $\alpha = 3°$ experimental data, (—) $\alpha = 9°$ LBM, (—) $\alpha = 9°$ experimental data, (—) $\alpha = 18°$ LBM, (—) $\alpha = 18°$ experimental data.

The comparison of these spectra evaluates the ability of LBM to model the phenomena observed in the experiment. In Fig. 11, the 3 degree angle in LBM appears to have a greater contribution at low frequencies and a rapid decrease at high frequencies. This evolution can be explained by the numerical representation of this case, in which the numerical boundary layer is less turbulent than in the wind tunnel. The wall-pressure spectrum at 9 degrees shows a similar evolution to that of the experiment. This phenomenon is also observed for the other angles. The peaks present at 9 degrees at 800 Hz and 18 degrees at 410 Hz are characteristic of incidence profile noise for a Strouhal number $St = fc\sin(\alpha)/U$ [4]. These peaks are slightly shifted due to the shift presented in Sec. 3.2.

4.2.2 Far-field acoustic spectra

The far-field noise is analyzed by comparing the spectra obtained from the experimental microphone array with those predicted by the LBM probes via direct acoustic propagation. In this paper the far-field spectra is shown as the parameter: s_{pp}. To ensure a proper comparison between LBM simulations and the experimental dataset, a correction is applied in Eq. 9. This correction is extracted from Soni et al.[18] and Fig. 12 presents representative far-field spectra for several static angles of attack.

$$PSD_{3D,\Delta_z} = PSD_{2.5D,slice} + 10\log_{10}\left(\frac{\Delta_z^2\ f}{c_0\ r}\right) \quad (9)$$

where Δ_z is the real span in the experiment and r the distance to the microphone from the airfoil.

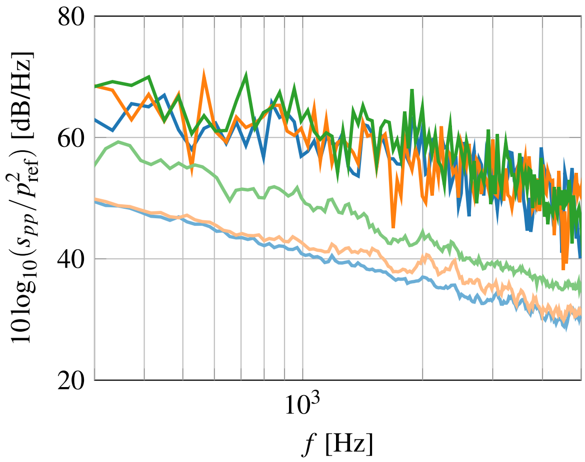

Figure 12. Comparison of far-field acoustic spectra between LBM and experiment at selected static angles of attack. (—) $\alpha = 3°$ LBM, (—) $\alpha = 3°$ experimental data, (—) $\alpha = 9°$ LBM, (—) $\alpha = 9°$ experimental data, (—) $\alpha = 18°$ LBM, (—) $\alpha = 18°$ experimental data.

A similar trend is observed between the phenomena present in the wall-pressure spectra in Sec. 4.2.1 and the far-field radiated noise in Fig. 12. The frequency shift is also found, as is the amplitude shift, for the same reasons as those mentioned in Sec. 4.2.1. The evolution of amplitude with the angle of attack is consistent between the wall spectra and the far-field noise, although a shift remains to be investigated in future simulations due to limited acquisition time.

4.3 Qualitative Identification of Acoustic Source Regions

Beyond the comparison of aerodynamic and acoustic integral quantities, the LBM simulations provide access to instantaneous flow and pressure fields, which can be exploited to gain qualitative insight into the localization of dominant acoustic source regions.

Instantaneous pressure fields reveal the presence of propagating pressure waves originating from the airfoil surface. To further investigate the spatial distribution of these sources, the Laplacian of pressure $\nabla^2 p$ and the dilatation field $\operatorname{div}(\mathbf{U})$, are examined. In compressible flow formulations, the pressure Laplacian and the dilatation field are commonly used as qualitative indicators of acoustic activity [19, 20].

Fig. 13 presents an instantaneous snapshot of the pressure Laplacian in the vicinity of the airfoil and Fig. 14 presents the instantaneous dilatation field and isocontours of Q-Criterion colored by vorticity magnitude. Two dominant source regions can be identified. The first one is located within the boundary layer developing on the suction side, where strong pressure gradients are associated with unsteady shear-layer dynamics and flow separation. The second source region is concentrated near the trailing edge, where the interaction between convected flow structures and the sharp edge leads to the radiation of pressure waves into the far-field.

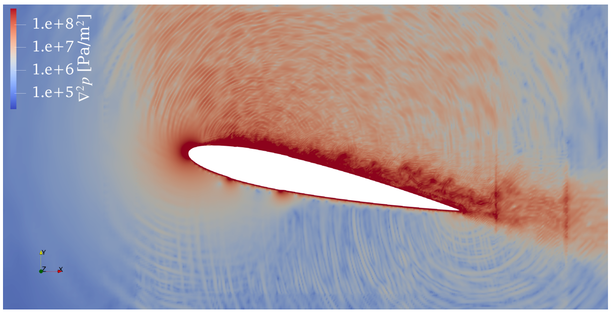

Figure 13. Instantaneous pressure Laplacian $\left(\nabla^2 p\right)$ at $\alpha = 12°$.

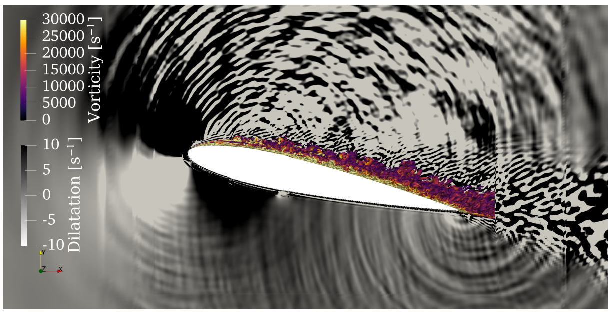

Figure 14. Dilatation field div$(\mathbf{U})$ and isocontours of Q-Criterion colored by vorticity, at $\alpha = 12°$.

Although this analysis remains qualitative, the identified source locations are consistent with classical interpretations of airfoil self-noise generation, in which boundary-layer turbulence and trailing-edge scattering play a dominant role [4, 20].

5. AERODYNAMICS AND ACOUSTICS OF A PITCHING AIRFOIL

Following the static analysis, the comparison is extended to the dynamic case corresponding to a periodic pitching motion of the airfoil. Dynamic stall is characterized by strong flow unsteadiness, delayed separation, and pronounced hysteresis effects, which significantly affect both aerodynamic loads and noise generation [2, 3, 21]. Both aerodynamics and acoustics are analyzed and compared to the experimental dataset obtained during the same measurement campaign. The dynamic case is described by a sinusoidal pitching motion of the jet at 4 Hz about a mean angle of 15° with an amplitude of ±7° centered on the airfoil.

5.1 Aerodynamics

The unsteady aerodynamic behavior is characterized by the evolution of the lift coefficient as a function of the instantaneous angle of attack. The resulting lift hysteresis loop constitutes a classical indicator of delayed reattachment [3, 21]. Fig. 15 presents the lift hysteresis loop obtained from the LBM simulations and the experimental measurements.

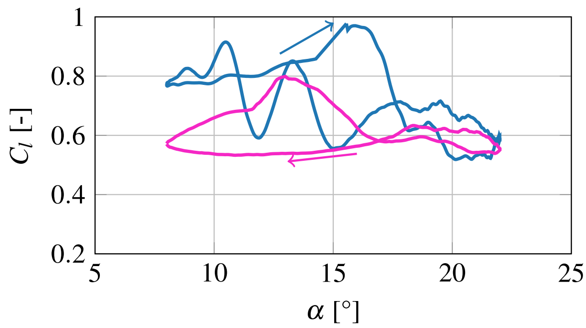

Figure 15. Lift coefficient hysteresis as a function of angle of attack for the dynamic pitching case: comparison between LBM predictions (——) and experimental data. (——)

The lift hysteresis loop is in good overall agreement between LBM and experimental data. The amplitude of C_l is slightly overestimated in LBM in the attached regime and the stall point is estimated at higher angle of attack in the LBM. However, LBM shows a good agreement at $\alpha \geq 18°$. Such behavior is consistent with previous numerical studies of dynamic stall based on high-fidelity simulation approaches [22].

5.2 Acoustics

The acoustics is analyzed through both wall-pressure spectra and far-field acoustic spectra. Unsteady separation and reattachment are known to induce strong temporal modulations of noise levels during dynamic stall [5, 6]. Fig. 16 shows the wall-pressure spectrum, while Fig. 17 presents the corresponding far-field acoustics.

The shape of the wall-pressure spectra spectrum is well reproduced by the LBM. In particular, the peak frequency at 400 Hz is representative of the boundary layer unsteadiness at a mean angle of $\alpha = 15°$, which leads to a Strouhal number of $St = 0.17$. The slope of the spectrum at high frequencies is also captured by the LBM.

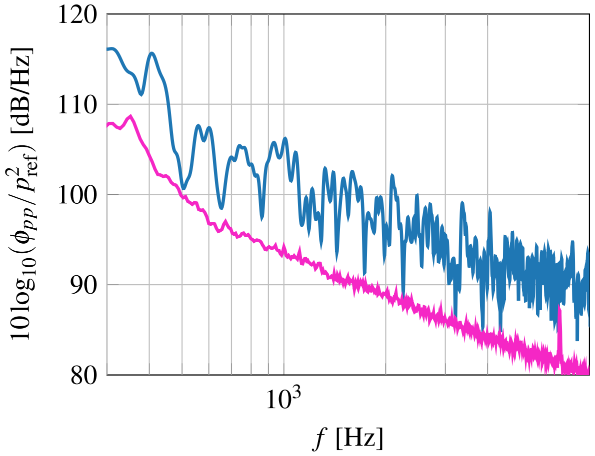

Figure 16. Wall-pressure spectrum on suction side at $x/c = 0.92$, during the dynamic pitching cycle: comparison between LBM (——) and experimental data (——).

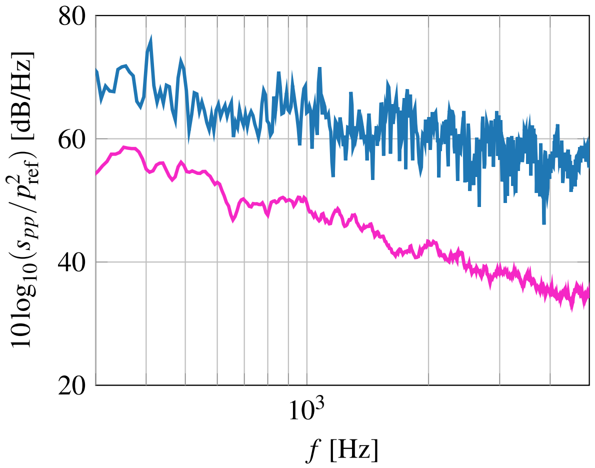

Figure 17. Far-field acoustic spectrum during the dynamic pitching cycle: comparison between LBM (——) and experimental data (——).

Concerning the far-field spectrum, the shape is also well reproduced by the LBM. The peak is less visible in the experiment, probably due to spanwise effect. These results demonstrate the capability of the LBM solver to capture both the unsteady aerodynamic loading and its acoustic consequences under dynamic stall conditions, in line with previous acoustic studies [17].

6. CONCLUSION

The present study investigated the ability of the Lattice Boltzmann Method to predict the aerodynamics and acoustics of a NACA0012 airfoil under static and dynamic stall conditions. Numerical simulations were performed at a Reynolds number of $Re_c = 6.25 \times 10^5$ and a Mach number of $Ma = 0.21$, and systematically compared to experimental measurements obtained during the same measurement campaign.

For the static configuration, the comparison of pressure coefficient distributions over a wide range of angles of attack demonstrated that the LBM solver reproduces the main aerodynamic trends observed experimentally, from attached flow to fully separated conditions. A systematic offset between numerical and experimental results was identified and attributed to a difference between the nominal geometric angle of attack and the effective aerodynamic incidence in the experiment. Once this offset is taken into account, a good agreement is obtained in terms of pressure distributions, lift curve slope and stall angle. The corresponding far-field acoustics is also well captured, with consistent trends in broadband noise levels and spectral content.

The analysis was then extended to a dynamic pitching configuration representative of dynamic stall conditions. The LBM simulations reproduced the characteristic lift hysteresis observed experimentally, including the delayed stall and reattachment phenomena. In addition, the wall-pressure and far-field acoustic spectra were shown to be consistent between the numerical and experimental datasets, demonstrating the capability of the LBM approach to capture the coupling between unsteady aerodynamics and noise generation.

Beyond integral quantities, the availability of instantaneous flow and pressure fields in the LBM simulations enabled a qualitative identification of the dominant acoustic sources. The analysis of the pressure Laplacian revealed that pressure waves originate primarily from the boundary layer developing along the suction side and from the trailing-edge region, in agreement with classical interpretations of airfoil self-noise mechanisms. Although qualitative, these observations provide additional confidence in the physical relevance of the numerical predictions.

Overall, the results presented in this work indicate that the Lattice Boltzmann Method constitutes a reliable and efficient approach for the simulation of aerodynamic and acoustic phenomena associated with static and dynamic stall at moderate Mach numbers. The level of agreement obtained with experimental data supports its application to more complex unsteady configurations, such as wind-turbine blades or rotating machinery components, where stall-related noise plays a critical role. Future work will focus on extending the present methodology to three-dimensional configurations and on further investigating the sensitivity of stall-noise mechanisms to unsteady inflow conditions.

7. ACKNOWLEDGMENT

This material is based upon work supported by the ANRT (Association nationale de la recherche et de la technologie) with a CIFRE fellowship granted to Milo Grimberg.

This work was granted access to the HPC resources of PMCS2I (Pôle de Modélisation et de Calcul en Sciences de l'Ingénieur de l'Information) of the École Centrale de Lyon, Écully, France. This project was provided with computing and storage resources by GENCI at TGCC thanks to the grant 2025-A018A14163 on the supercomputer Joliot Curie's ROME partition.

REFERENCES

[1] PIBE Consortium. PIBE: Prévoir l'impact du bruit des éoliennes. French National Research Agency (ANR) project, 2017–2021. ANR project focused on aerodynamic and aeroacoustic characterization of wind-turbine airfoils, ANR-16-CE22-0004.

[2] W. J. McCroskey. The phenomenon of dynamic stall. Technical Report TM-81264, NASA, 1981.

[3] L. W. Carr. Progress in analysis and prediction of dynamic stall. *AIAA Journal*, 26(9):1041–1052, 1988.

[4] T. F. Brooks, D. S. Pope, and M. A. Marcolini. Airfoil self-noise and prediction. Technical Report RP-1218, NASA, 1989.

[5] D. Raus, B. Cotté, R. Monchaux, L. Sicard, E. Jondeau, P. Souchotte, and M. Roger. Experimental characterization of the noise generated by an airfoil oscillating above stall. In *AIAA AVIATION 2021 FORUM*, VIRTUAL EVENT, August 2021. American Institute of Aeronautics and Astronautics.

[6] D. Raus, B. Cotté, R. Monchaux, E. Jondeau, P. Souchotte, and M. Roger. Experimental study of the dynamic stall noise on an oscillating airfoil. *Journal of Sound and Vibration*, 537:117144, October 2022.

[7] P. Lallemand and L.-S. Luo. Theory of the lattice boltzmann method: Acoustic and thermal properties in two and three dimensions. *Physical Review E*, 61(6):6546–6562, 2000.

[8] D. Casalino, E. Fares, and W. Schroeder. Towards accurate lattice boltzmann aeroacoustics. *AIAA Journal*, 52(1):86–96, 2014.

[9] A. Suss, I. Mary, T Le Garrec, and S Marié. Comprehensive comparison between the lattice boltzmann and navier–stokes methods for aerodynamic and aeroacoustic applications. *Computers & Fluids*, 257:105881, 2023.

[10] CS GROUP. High-fidelity lattice boltzmann cfd simulations — prolb. https://www.prolb-cfd.com/.

[11] O. Malaspinas. Increasing stability and accuracy of the lattice boltzmann scheme: recursivity and regularization. *arXiv preprint*, 2015.

[12] J. Jacob, O. Malaspinas, and P. Sagaut. A new hybrid recursive regularised bhatnagar–gross–krook collision model for lattice boltzmann method-based large eddy simulation. *Journal of Turbulence*, 19(11-12):1051–1076, 2018.

[13] I. H. Abbott and A. E. von Doenhoff. *Theory of Wing Sections*. Dover Publications, 1949.

[14] J. D. Anderson. *Fundamentals of Aerodynamics*. McGraw-Hill, 5 edition, 2011.

[15] P. R. Spalart and S. R. Allmaras. A one-equation turbulence model for aerodynamic flows. *La Recherche Aérospatiale*, 1:5–21, 1994.

[16] I. Mary and P. Sagaut. Large eddy simulation of flow around an airfoil using the lattice boltzmann method. *Physics of Fluids*, 27(2):025103, 2015.

[17] A. Ribeiro, D. Casalino, and E. Fares. Lattice-boltzmann simulations of an oscillating naca0012 airfoil in dynamic stall. In M. Braza, A. Bottaro, and M. Thompson, editors, *Advances in Fluid-Structure Interaction*, pages 179–192, Cham, 2016. Springer International Publishing.

[18] M. Soni, R. Ewert, J. Delfs, and K. Masilamani. *Towards Wall-Modeled LES with Lattice Boltzmann Method for Aeroacoustics: Application and Understanding*.

[19] M. J. Lighthill. On sound generated aerodynamically. i. general theory. *Proceedings of the Royal Society of London. Series A*, 211(1107):564–587, 1952.

[20] M. S. Howe. *Acoustics of Fluid-Structure Interactions*. Cambridge University Press, 1998.

[21] J. G. Leishman. *Principles of Helicopter Aerodynamics*. Cambridge University Press, 2006.

[22] M. R. Visbal and D. J. Garmann. Analysis of dynamic stall on a pitching airfoil using large-eddy simulation. *Journal of Fluid Mechanics*, 862:836–873, 2019.